



Short communication

In operando X-ray diffraction study of Li_7MnN_4 upon electrochemical Li extraction–insertion: A reversible three-phase mechanism

N. Emery^{a,*}, E. Panabière^a, O. Crosnier^{b,c}, S. Bach^{a,d}, T. Brousse^{b,c}, P. Willmann^e, J.-P. Pereira-Ramos^a

^a Institut de Chimie et des Matériaux Paris-Est, GESMAT, UMR 7182 CNRS – Université Paris Est Créteil, 2, rue Henri-Dunant, 94320 Thiais, France

^b IMN, UMR6502 La Chantrerie, rue Christian Pauc, 44306 Nantes, France

^c RS2E, FR3459 CNRS, France

^d Université d'Evry Val d'Essonne, Département Chimie, Bd François Mitterrand, 91025 Evry Cedex, France

^e Centre National d'Etudes Spatiales, 18 avenue Edouard Belin, 31401 Toulouse Cédex 9, France

HIGHLIGHTS

- First in operando XRD study of a nitride upon electrochemical Li extraction/insertion.
- 3 phase mechanism of Li_7MnN_4 involving two biphasic domains and one solid solution.
- Reversible strain induced by Li extraction observed from XRD peak profile broadening.

ARTICLE INFO

Article history:

Received 6 June 2013

Received in revised form

19 July 2013

Accepted 3 August 2013

Available online 11 September 2013

Keywords:

Li-ion batteries

Anode material

In operando XRD

Lithiated transition metal nitride

ABSTRACT

The Li_7MnN_4 structural response upon the first Li extraction–insertion cycle is highlighted using in operando XRD experiments. A 3-phases mechanism involving two biphasic regions for $0.1 \leq x \leq 0.8$ and $0.8 \leq x \leq 1.2$ in $\text{Li}_{7-x}\text{MnN}_4$ and a solid solution behaviour ($1.2 \leq x \leq 1.5$) explains its electrochemical fingerprint. These successive structural transitions do not change the cubic symmetry of the cell and induce a limited cell contraction ($\sim 7\%$) associated to a reversible mechanical strain. This finding partly explains the excellent cycle life of this promising negative electrode for Li-ion batteries.

© 2013 Elsevier B.V. All rights reserved.

1. Introduction

During the past 20 years, ternary transition metal nitrides were the subject of many studies devoted to energy storage [1]. Among a wide variety of composition, Li_7MnN_4 appears as a potential Li-ion batteries anode material with a specific capacity between 235 and 285 mA h g^{-1} available at $\approx 1.2 \text{ V}$ vs Li/Li^+ [2–5]. During the charge process leading to $\text{Li}_{7-x}\text{MnN}_4$ with $0 < x \leq 1.4/1.7$ [2–5], oxidation of Li_7MnN_4 gives rise to a long voltage plateau centred around 1.2 V for $0 < x < 1$ followed by a strong increase of the potential for $x > 1$. Surprisingly, from a structural viewpoint, a quite small biphasic domain ($0.1 < x < 0.5$) followed by a wider solid-solution region

($0.625 < x < 1.25$) are reported in Ref. [4] while electrochemical data rather suggest a large biphasic domain followed by a narrow solid solution for $x > 1$ [2–5]. In other respects the presence of two very close discharge plateaus at $\approx 1.14 \text{ V}$ and $\approx 1.16 \text{ V}$ reported in some experiments suggests a more complex structural mechanism [3]. Therefore we decided to perform in operando XRD experiments at low C rate (C/20) to account at the best for the structural changes occurring in Li_7MnN_4 as electrochemical Li extraction–insertion proceeds. By this way, we have been able to elucidate the structural response of Li_7MnN_4 involving a 3-phase mechanism in good accord with the observed electrochemical properties.

2. Experimental

Li_7MnN_4 was prepared by solid state reaction under controlled atmosphere from reagent grade Li_3N (Alfa-Aesar 99.4%, -60 mesh)

* Corresponding author. Institut de Chimie et des Matériaux Paris-Est, GESMAT, UMR 7182 CNRS – Université Paris Est Créteil, 2, rue Henri-Dunant, 94320 Thiais, France.

E-mail address: emery@icmpe.cnrs.fr (N. Emery).

and Mn metal (Alfa-Aesar 99+%, –325 mesh). The powder mixture was thoroughly ground in an agate mortar and pressed into pellet (13 mm diameter and 6–8 mm thick). 20% excess of Li_3N regards to the stoichiometry ratio Li/Mn was added to compensate lithium evaporation during the thermal treatment. The pellet of about 1 g was then transferred in an alumina crucible enclosed in a tubular stainless steel reactor and heated during 7 h at 750 °C under a nitrogen gas stream. A second alumina boat filled with titanium sponge was also added to trap any oxygen and moisture traces present in the gas. All manipulations were carried out in an argon glove box. The synthesis product was characterized by X-ray diffraction (XRD) using a Bruker D8 Advance diffractometer with LynxEye detector and $\text{Cu K}\alpha$ radiation. A 4 h acquisition performed using an air-tied sample holder in the 2θ range 18–110° (step size of 0.01023°) is presented in Fig. 1.

A Rietveld refinement to control the sample quality was performed with GSAS software [6,7]. A derivative anti- CaF_2 type cubic structure (P-43n space group) [8] well describes the diagram with excellent agreement factors ($\chi^2 = 1.308$, $wRp = 2.18\%$ and $Rp = 1.67\%$). The cell parameter reaches 9.5582(1) Å accordingly with literature [2,4,9]. No impurity has been detected. This structural model, which contains 8 formula units, is drawn in Fig. 2 with the nitrogen tetrahedra filled by the Mn^{5+} ions. Also, elemental analysis of cationic species was performed and confirms the Li_7MnN_4 stoichiometry.

A modified Swagelok type electrochemical cell with a beryllium window described elsewhere [10] was used to record the in operando XRD patterns. In this two-electrode cell configuration, a lithium disk acts as both reference and counter electrodes. The working electrode is composed of 70% wt of active material, 22% wt of acetylene black and 8% wt of PTFE as binding agent. Such paste was pressed on a copper grid disk (12 mm diameter, Goodfellow) and placed next to the Be window. The separator was a Whatman™ paper disk soaked with LP71 electrolyte from BASF (1 mol L^{-1} LiPF_6 in ethylene carbonate/diethyl carbonate/dimethyl carbonate, 1:1:1, v/v). The initial charge was performed at the slow rate of C/30 in the potential range 1/1.6 V (i.e. 30 h to accomplish the full discharge) followed by a subsequent discharge at the same C-rate using a VSP Biologic. 30 min scans were recorded between 16 and 58° in 2θ -range (step size of 0.017°) using a Panalytical Xpert Pro diffractometer equipped with an X'celerator detector and a $\text{Cu K}\alpha$ radiation. To precisely analyse the structural data vs x in $\text{Li}_{7-x}\text{MnN}_4$, one XRD pattern is recorded every 30 min, i.e. every $\Delta x = 0.025$ in $\text{Li}_{7-x}\text{MnN}_4$. Such a short acquisition time has been chosen to obtain good compromise between XRD pattern resolution and a negligible variation of Li content in the sample.

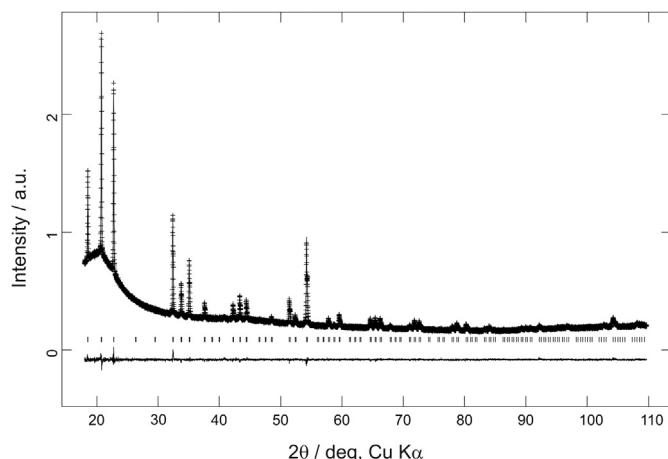


Fig. 1. Rietveld refinement of Li_7MnN_4 XRD pattern.

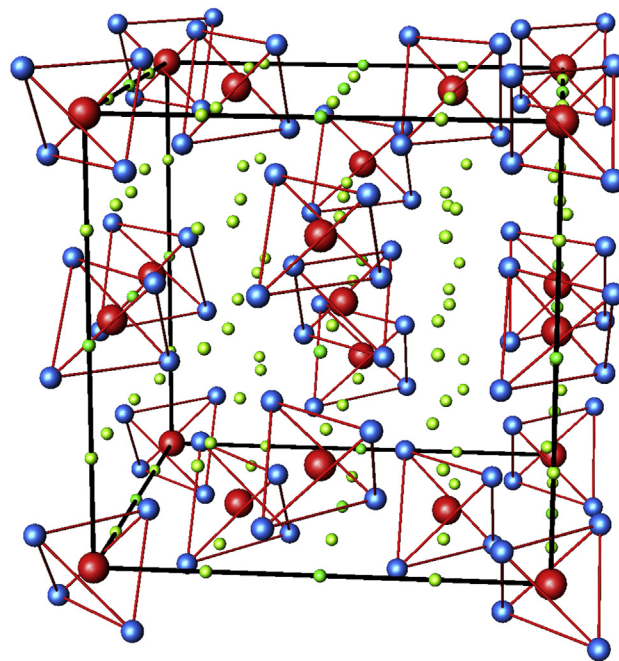
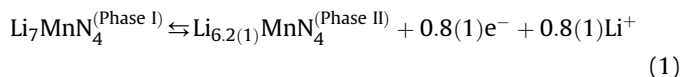


Fig. 2. Crystallographic structure of Li_7MnN_4 (cubic cell with P-43n space group, $a = 9.558$ Å). Li, Mn, N are green, red and blue spheres respectively. (For interpretation of the references to colour in this figure legend, the reader is referred to the web version of this article.)

3. Results and discussion

Fig. 3a and 3b gather the XRD patterns collected during the oxidation and reduction of Li_7MnN_4 with the corresponding charge and discharge curves. Only the 31–37° and 53.5–56.5° 2θ ranges are plotted to account for the structural response of Li_7MnN_4 . Full patterns are available in ESI S1. Blue stars at 54.7 and 55.5° in Fig. 3 indicate small reflexions attributed to the cell design and their intensities remain constant during all the experiment. A sharp potential increase from 1.15 to 1.2 V is observed for $x < 0.1$ i.e. when the first Li ions are extracted, followed by a long voltage plateau near 1.2 V involving about 1 additional Li ion. Then a significant increase in the working voltage occurs from 1.22 V to 1.6 V for $1 < x < 1.5$. Very early, i.e. for $x \geq 0.1$, XRD patterns clearly indicate the emergence of shoulders at higher angles for all Li_7MnN_4 peaks (Fig. 3a). Such splitting suggests the appearance of a second cubic phase, with a smaller cell parameter. The intensity of these new peaks is continuously growing upon further Li deintercalation to reach a maximum value at $x \approx 0.8$. In the same time, the Li_7MnN_4 peaks intensity decreases with x in $\text{Li}_{7-x}\text{MnN}_4$ and vanishes around $x \approx 0.8$. The chemical composition of the second phase is by the way estimated close to $\text{Li}_{6.2(1)}\text{MnN}_4$. In a few words, Li_7MnN_4 and $\text{Li}_{6.2(1)}\text{MnN}_4$ (labelled I and II respectively in Fig. 3) coexist for $0.1 \leq x \leq 0.8$ owing to the following reaction:



For $x > 0.8$, a new set of peaks arises, once again at higher 2θ values, suggesting another phase transition leading to a cubic cell with a smaller parameter (noted III in Fig. 3). Their intensity is continuously growing with x at the expense of phase II. A second biphasic domain involving phases II and III is evidenced for $0.8 \leq x \leq 1.2$, i.e. until the complete disappearance of the second phase. This process can be written according to Equation (2).

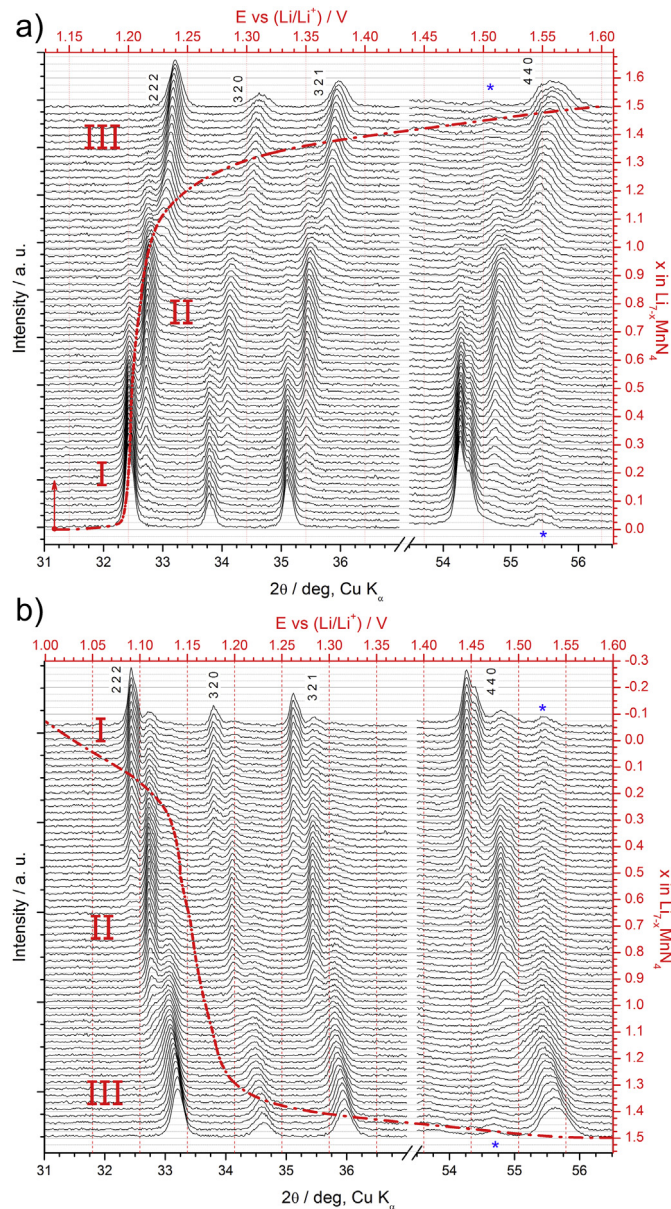
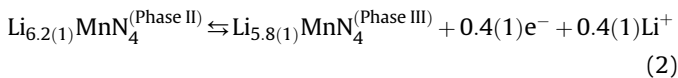
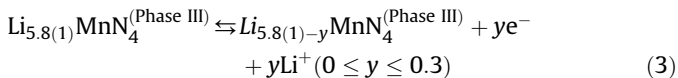


Fig. 3. XRD patterns (black axes) and galvanostatic curves (red axes) recorded during the (a) oxidation/(b) reduction of $\text{Li}_{7-x}\text{MnN}_4$ at C/20 rate. Stars at 54.7 and 55.5° are attributed to the cell design (not involved in the process). (For interpretation of the references to colour in this figure legend, the reader is referred to the web version of this article.)



A very short one-phase domain should exist since a single phase was found for $x \approx 0.8$ ($\text{Li}_{6.2(1)}\text{MnN}_4$). However the limits of this monophasic region have not been clearly evidenced in our conditions. Finally, a solid-solution domain from $x \approx 1.2$ to the maximum extracted lithium amount completes the oxidation process up to 1.6 V leading to $\text{Li}_{5.5}\text{MnN}_4$ (phase III, Equation (3)).



Indeed, in this Li composition range, all the diffraction peaks slowly shift to higher angles according to a progressive cell volume contraction.

The set of peaks attributed to the second phase $\text{Li}_{6.2(1)}\text{MnN}_4$ is easily indexed using the same space group than Li_7MnN_4 , i.e. P-43n with a cell parameter of $9.465(4)$ Å in agreement with preliminary XRD studies [2,4]. As described above, a third phase not yet observed originates from x close to 0.8 with an initial lower cubic cell parameter a of $9.358(1)$ Å. For $x > 1.2$, the solid solution of the third phase induces a contraction of the cell parameter down to $a = 9.331(1)$ Å at the end of the oxidation process.

The cell parameter and volume of each phase evidenced during the charge reaction are reported in Fig. 4 as a function of x in $\text{Li}_{7-x}\text{MnN}_4$. As seen from Fig. 4, a first extended biphasic domain occurs (~ 0.1 – 0.8) immediately followed by the second biphasic domain (~ 0.8 – 1.2). The last step is the solid-solution behaviour of the third phase characterized by the continuous contraction of the cell parameter with the deintercalated lithium amount up to 1.5. In a few words, Li removal leads to the new composition $\text{Li}_{5.5}\text{MnN}_4$ with a cell contraction of $\sim 7\%$.

The structural transformations observed during the oxidation step are reversible during the discharge process as it is demonstrated in Fig. 3b. Indeed, lithium accommodation induces the successive appearance of two sets of peaks at lower angles showing an increase in the cubic cell parameter. This trend is exactly the symmetric finding observed for the charge process. The same comments can be made for the composition ranges of the one-phase and two-phase regions showing the high reversibility of these structural changes. When phase III, i.e. $\text{Li}_{5.5(1)}\text{MnN}_4$ is enriched with Li ions during discharge (Equation (3)), the cell parameter increases from $9.331(1)$ Å up to $9.358(1)$ Å for $x \approx 1.2$. Then, a short biphasic area ($0.8 \leq x \leq 1.2$) takes place again with $\text{Li}_{6.2(1)}\text{MnN}_4$ (phase II) until the full disappearance of phase III (Equation (2)). Li_7MnN_4 grows within the reduction of $\text{Li}_{6.2(1)}\text{MnN}_4$ amount in the large biphasic area observed between $0 \leq x \leq 0.8$ in $\text{Li}_{7-x}\text{MnN}_4$ (Equation (1)). However, a very small amount of $\text{Li}_{6.2(1)}\text{MnN}_4$ is still present at 1 V.

A meaningful experimental finding is the progressive broadening of the diffraction peaks occurring with x in $\text{Li}_{7-x}\text{MnN}_4$ (Fig. 3a). This trend is indicative of an increasing disorder and/or a reduction of coherent domains. This peak broadening is reversible during the subsequent electrochemical Li insertion as seen in Fig. 3b. The analysis of the mechanical strain and the crystallite

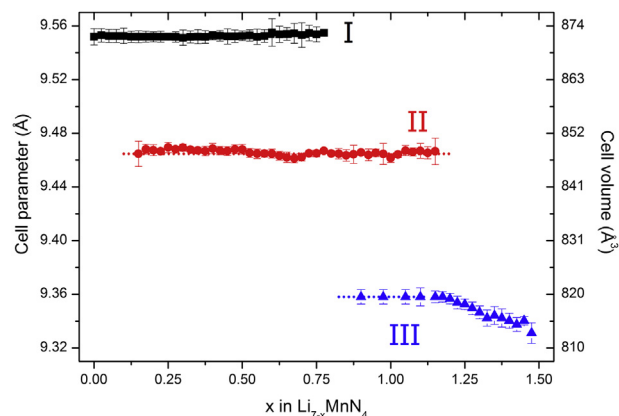


Fig. 4. Evolution of the cell parameter of the three cubic phases observed upon lithium extraction.

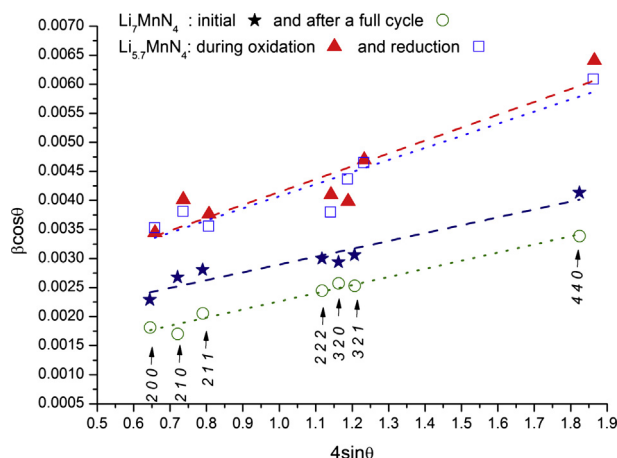


Fig. 5. Williamson–Hall plots for Li_7MnN_4 , $\text{Li}_{5.7}\text{MnN}_4$ and after a full cycle.

size during the Li extraction–insertion reaction is performed using the simple Williamson–Hall (W–H) approach [11]. Indeed, the peak breath (noted β_{hkl}) variation can be related to the crystallite size D and the mechanical strain ε according to the following formula:

$$\beta_{hkl} \cos \theta = K\lambda/D + 4\varepsilon \sin \theta \quad (4)$$

where K is the shape factor (fixed to 0.9) and λ the wavelength. A set of plots of $\beta_{hkl} \cos \theta$ vs. $4 \sin \theta$ for several diffraction peaks is drawn in Fig. 5 for Li_7MnN_4 , before and after the full cycle, and also for $\text{Li}_{5.7}\text{MnN}_4$ (phase III) achieved during the charge and discharge. According to Equation (1), the slope and the y-intercept of each straight line give an estimation of the strain ε and the crystallite size D respectively. For pristine Li_7MnN_4 , D is estimated around 900 Å and ε reaches 0.135%. For phase III, $\text{Li}_{5.7}\text{MnN}_4$, obtained during oxidation and reduction the slope, i.e. the lattice strain, is almost twice that found for the pristine material with values around 0.2%. The crystallite sizes remain in the same order of magnitude, with values slightly lower close to 700 Å. After a full charge–discharge cycle, the mechanical strain ($\varepsilon \approx 0.14\%$) retrieves the value found for the pristine material. $\text{Li}_{6.2(1)}\text{MnN}_4$ traces impede any reliable determination of the crystallite size. However, the initial crystallinity of Li_7MnN_4 characterized by sharp and well defined diffraction peaks is clearly recovered after a full charge–discharge cycle.

4. Conclusion

In summary, the structural response of Li_7MnN_4 upon extraction/insertion is driven by the existence of three cubic phases and their existence domains have been determined as a function of x in $\text{Li}_{7-x}\text{MnN}_4$. The present new structural data satisfactorily explain the electrochemical behaviour of Li_7MnN_4 by the existence of two biphasic regions and a solid-solution behaviour with a cell volume variation limited to 7% and reversible mechanical strain which is favourable to an excellent cycling life. Additional experiments are required to fully describe the redox mechanisms involved in this promising negative electrode material for Li-ion batteries [12,13].

Acknowledgement

Financial support from the ANR has been appreciated within the project Advanced NiBaCa. We are indebted to F. GUILLOU and P. SOUDAN for technical support. M. WEISSMANN is warmly acknowledged for his valuable help.

Appendix A. Supplementary data

Supplementary data related to this article can be found at <http://dx.doi.org/10.1016/j.jpowsour.2013.08.008>.

References

- [1] J.M. Cameron, R.W. Hughes, Y. Zhao, D.H. Gregory, *Chem. Soc. Rev.* 40 (2011) 4099.
- [2] J. Cabana, N. Dupré, G. Rousse, C. Grey, M.R. Palacín, *Solid State Ionics* 176 (2005) 225.
- [3] J. Cabana, G. Rousse, M.R. Palacín, in: C. Julien, K. Zaghib, J. Prakash (Eds.), *New Trends in Intercalation Compounds for Energy Storage and Conversion*, The Electrochemical Society Proceeding Series: Paris, 2003, p. 139. PV2003-20.
- [4] M. Nishijima, N. Tadokoro, Y. Takeda, N. Imanishi, O. Yamamoto, *J. Electrochem. Soc.* 141 (1994) 2966.
- [5] S. Suzuki, T. Shodai, *Solid State Ionics* 116 (1999) 1.
- [6] A.C. Larson, R.B. Von Dreele, *General Structure Analysis System (GSAS)*. Technical Report LAUR86-748, Los Alamos National Laboratory, 2004.
- [7] B.H. Toby, *J. Appl. Crystallogr.* 34 (2001) 210.
- [8] R. Juza, E. Anschutz, H. Puff, *Angew. Chem.* 71 (1959) 161.
- [9] R. Niewa, F.R. Wagner, W. Schnelle, O. Hochrein, R. Kniep, *Inorg. Chem.* 40 (2001) 5215.
- [10] J.B. Leriche, S. Hamelet, J. Shu, M. Morcrette, C. Masquelier, G. Ouvrard, M. Zerrouki, P. Soudan, S. Belin, E. Elkaïm, F. Baudelet, *J. Electrochem. Soc.* 157 (2010) A606.
- [11] V.D. Mote, Y. Purushotham, B.N. Dole, *J. Theor. Appl. Phys.* 6 (2012) 6.
- [12] E. Panabière, N. Emery, S. Bach, J.-P. Pereira-Ramos, P. Willmann, *Electrochim. Acta* 97 (2013) 393.
- [13] J. Cabana, C.M. Ionica-Bousquet, C.P. Grey, M.R. Palacín, *Electrochem. Commun.* 12 (2010) 315–318.